Autophagy Defends Cells Against Invading Group A Streptococcus

Ichiro Nakagawa, *et al.*

Science **306**, 1037 (2004);
DOI: 10.1126/science.1103966

Ligands and Peptide Motifs (Landes Bioscience, Georgetown, TX, 1997).
15. P. B. Singh, R. E. Brown, B. Roser, *Nature* **327**, 161 (1987).
16. T. Boehm, C. C. Bleul, M. Schorpp, *Immunol. Rev.* **195**, 15 (2003).
17. Materials and methods are available as supporting material on *Science* Online.
18. Single-letter abbreviations for the amino acid residues are as follows: A, Ala; C, Cys; D, Asp; E, Glu; F, Phe; G, Gly; H, His; I, Ile; K, Lys; L, Leu; M, Met; N, Asn; P, Pro; Q, Gln; R, Arg; S, Ser; T, Thr; V, Val; W, Trp; and Y, Tyr.
19. P. Lucas, K. Ukhanov, T. Leinders-Zufall, F. Zufall, *Neuron* **40**, 551 (2003).
20. S. M. Potter *et al.*, *J. Neurosci.* **21**, 9713 (2001).
21. M. Spehr, H. Hatt, C. H. Wetzel, *J. Neurosci.* **22**, 8429 (2002).
22. Y. E. Lau, J. A. Cherry, *Neuroreport* **11**, 27 (2000).
23. T. Leinders-Zufall *et al.*, data not shown.
24. S. Martini, L. Silvotti, A. Shirazi, N. J. Ryba, R. Tirindelli, *J. Neurosci.* **21**, 843 (2001).
25. D. J. Speca *et al.*, *Neuron* **23**, 487 (1999).
26. H. M. Bruce, *Nature* **184**, 105 (1959).
27. A. Lloyd-Thomas, E. B. Keverne, *Neuroscience* **7**, 907 (1982).
28. The efficiency of pregnancy block by direct application of unfamiliar urine is similar to that caused by the presence of unfamiliar mice (for instance, when BALB/c females are mated with C57BL/6 males, presence of BALB/c males causes pregnancy failure in 9 of 12 mice).
29. R. J. O'Connell, M. Meredith, *Behav. Neurosci.* **98**, 1083 (1984).
30. T. Ishii, J. Hirota, P. Mombaerts, *Curr. Biol.* **13**, 394 (2003).
31. J. Loconto *et al.*, *Cell* **112**, 607 (2003).
32. X. L. He, P. Tabaczewski, J. Ho, I. Stroynowski, K. C. Garcia, *Structure* **9**, 1213 (2001).
33. D. Penn, W. Potts, *Adv. Immunol.* **69**, 411 (1998).
34. G. K. Beauchamp, K. Yamazaki, *Biochem. Soc. Trans.* **31**, 147 (2003).
35. J. L. Hurst *et al.*, *Nature* **414**, 631 (2001).

36. We thank R. Escher for peptide synthesis, J. Cherry for PDE4A antibodies, R. Tirindelli for V2R2 antibodies, P. Mombaerts for OMP-GFP mice, and K. Kelliher for the demonstration that nonvolatile chemicals can reach the VNO in vivo. This work was supported by the Leibniz program of the Deutsche Forschungsgemeinschaft (T.B. and H.B.), by NIH/National Institute on Deafness and other Communication Disorders (T.L.-Z. and F.Z.), and by the Hochshul- und Wissenschafts-Programm (P.W.).

Supporting Online Material

www.sciencemag.org/cgi/content/full/306/5698/1033/DC1
Materials and Methods
SOM Text
Figs. S1 to S4
Table S1
References

15 July 2004; accepted 9 September 2004

Autophagy Defends Cells Against Invading Group A *Streptococcus*

Ichiro Nakagawa,[1,3]* Atsuo Amano,[2,4] Noboru Mizushima,[3,5] Akitsugu Yamamoto,[6] Hitomi Yamaguchi,[7] Takahiro Kamimoto,[7] Atsuki Nara,[6,7] Junko Funao,[1] Masanobu Nakata,[1] Kayoko Tsuda,[7] Shigeyuki Hamada,[1] Tamotsu Yoshimori[4,7]*

We found that the autophagic machinery could effectively eliminate pathogenic group A *Streptococcus* (GAS) within nonphagocytic cells. After escaping from endosomes into the cytoplasm, GAS became enveloped by autophagosome-like compartments and were killed upon fusion of these compartments with lysosomes. In autophagy-deficient Atg5$^{-/-}$ cells, GAS survived, multiplied, and were released from the cells. Thus, the autophagic machinery can act as an innate defense system against invading pathogens.

Autophagy mediates the bulk degradation of cytoplasmic components in eukaryotic cells in which a portion of the cytoplasm is sequestered in an autophagosome and eventually degraded upon fusion with lysosomes (*1*–*3*). *Streptococcus pyogenes* (also known as group A *Streptococcus*, GAS) is the etiological agent for a diverse collection of human diseases (*4*). GAS invades nonphagocytic cells (*5*, *6*), but the destination of GAS after internalization is not well understood. To clarify the intracellular fate of GAS, especially any possible involvement of autophagy, we first investigated whether intracellular GAS colocalizes with LC3, an autophagosome-specific membrane marker, following invasion of HeLa cells (*7*–*9*). After infection, GAS strain JRS4 cells colocalized with LC3-positive vacuole-like structures in HeLa cells (Fig. 1A). The size (5 to 10 μm) and morphology of the structures were distinct from standard starvation-induced autophagosomes with a diameter of about 1 μm (fig. S1A), so we designated these structures GAS-containing LC3-positive autophagosome-like vacuoles (GcAVs). The number of cells bearing GcAVs, the area of GcAVs, and ratio of GAS trapped in GcAVs to total intracellular GAS increased in a time-dependent manner, reaching a maximum at 3 hours after infection (Fig. 1, B and C; figs. S1B and S2A). A similar result was obtained in mouse embryonic stem (ES) cells (figs. S2B and S3A). About 80% of intracellular GAS were eventually trapped by the compartments (Fig. 1C; fig. S1B). LC3 frequently surrounded GAS, fitting closely around a GAS chain (Fig. 1, D and E; movie S1).

LC3 exists in two molecular forms. LC3-I (18 kD) is cytosolic, whereas LC3-II (16 kD) binds to autophagosomes (*7*, *8*). The amount of LC3-II, which directly correlates with the number of autophagosomes (*8*), increased after infection (Fig. 1F). Thus, GAS invasion appears to induce autophagy, specifically trapping intracellular GAS.

To substantiate this idea, we examined GcAV formation in Atg5-deficient (Atg5$^{-/-}$) cells lacking autophagosome formation (*7*). In contrast to the wild-type cells (fig. S2, B and C), no GcAVs were observed in Atg5$^{-/-}$ ES cells (J1-2) (Fig. 2A) or in Atg5$^{-/-}$ mouse embryonic fibroblasts (MEFs) (fig. S2C). Thus, GcAV formation requires an Atg5-mediated mechanism. We also examined LC3-II formation. During infection with GAS, Atg5$^{-/-}$ cells showed no induction of LC3-II (Fig. 2B). By electron microscopy, in wild-type MEF cells infected with GAS, we observed characteristic cisternae surrounding GAS in the cytoplasm (Fig. 2C). No GAS were found surrounded by the membranes in Atg5$^{-/-}$ cells (Fig. 2C). The autophagosome-like multiple membrane–bound compartment containing GAS was also found in HeLa cells (Fig. 2D).

Next, we asked whether the bacteria are killed or survive after entering the compartments. To address this question, we directly scored bacterial viability by counting colony-forming units (CFU viability assay) in wild-type and Atg5$^{-/-}$ MEFs (Fig. 2E). In wild-type MEFs at 4 hours after infection, intracellular GAS had been killed (Fig. 2E), whereas the decrease of GAS viability was suppressed in the Atg5$^{-/-}$ MEFs. Tannic acid is a cell-impermeable fixative that prevents fusion between secretory vesicles and the plasma membrane but does not affect intracellular membrane trafficking (*10*). In Atg5$^{-/-}$ cells treated with tannic acid to prevent external escape of GAS, the viable bacteria increased by 2 hours after infection and maintained this level at 4 hours after infection (Fig. 2E). In contrast, the numbers of intracellular GAS decreased rapidly in tannic acid–treated wild-type cells as well

[1]Department of Oral and Molecular Microbiology, [2]Department of Oral Frontier Biology, Osaka University Graduate School of Dentistry, 1-8 Yamadaoka, Suita-Osaka 565-0871, Japan. [3]PRESTO, [4]CREST, Japan Science and Technology Agency, Kawaguchi-Saitama 332-0012, Japan. [5]Department of Bioregulation and Metabolism, The Tokyo Metropolitan Institute of Medical Science, 3-18-22 Honkomagome, Bunkyo-ku, Tokyo 113-8613, Japan. [6]Department of Cell Biology, Faculty of Bio-Science, Nagahama Institute of Bio-Science and Technology, 1266 Tamura-cho, Nagahama-Shiga 526-0829, Japan. [7]Department of Cell Genetics, National Institute of Genetics/SOKENDAI, Yata 1111, Mishima-Shizuoka 411-8540, Japan.

*To whom correspondence should be addressed. E-mail: ichiro@dent.osaka-u.ac.jp and tamyoshi@lab.nig.ac.jp

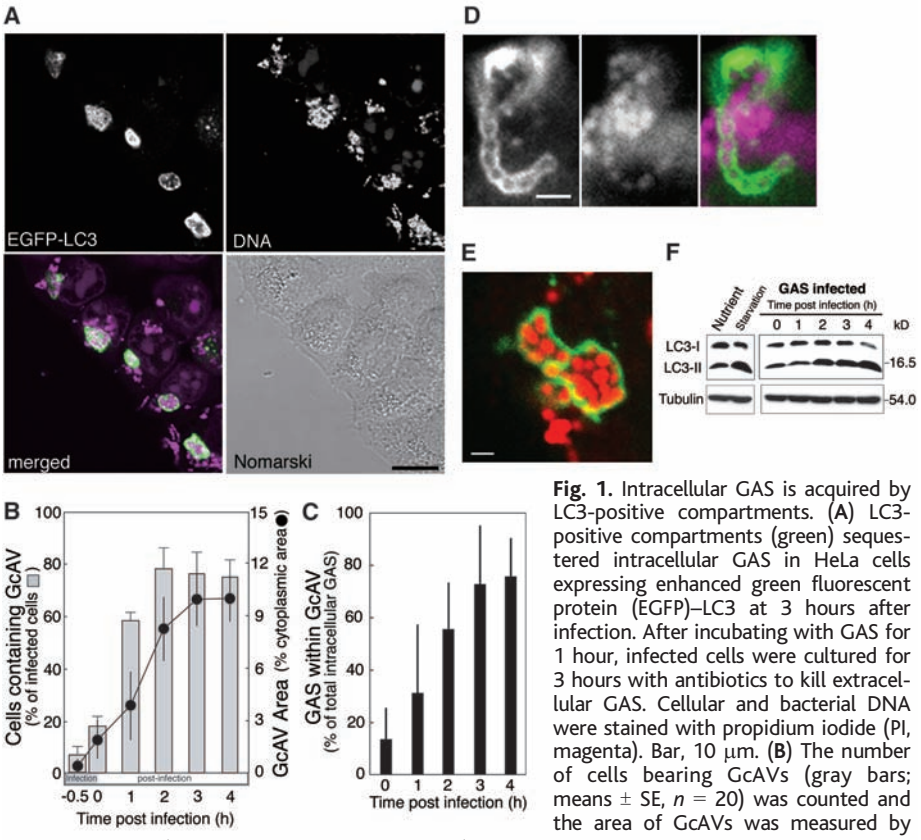

Fig. 1. Intracellular GAS is acquired by LC3-positive compartments. (**A**) LC3-positive compartments (green) sequestered intracellular GAS in HeLa cells expressing enhanced green fluorescent protein (EGFP)–LC3 at 3 hours after infection. After incubating with GAS for 1 hour, infected cells were cultured for 3 hours with antibiotics to kill extracellular GAS. Cellular and bacterial DNA were stained with propidium iodide (PI, magenta). Bar, 10 μm. (**B**) The number of cells bearing GcAVs (gray bars; means ± SE, $n = 20$) was counted and the area of GcAVs was measured by Image-J software (black circles; means ± SE, $n = 20$). The micrographs at each point are shown in fig. S1. (**C**) The total area of GAS within GcAVs was calculated as the percentage of total area of the invaded GAS. (**D**) High-resolution microscope image of a GcAV (green) and GAS (magenta) at 1 hour after infection. Bar, 2 μm. (**E**) Confocal microscopic image of a GcAV at 3 hours after infection (LC3, green; DNA, red). The three-dimensional image is available as movie S1. Bar, 2 μm. (**F**) Immunoblot analysis of LC3-II in GAS-infected HeLa cells. In (B) and (C), data are representative of at least three independent experiments.

as in untreated wild-type cells (Fig. 2E). GAS were not killed at all in the Atg5$^{-/-}$ cells, and some of the GAS were released from the cells, suggesting that the autophagic machinery can kill intracellular GAS and helps prevent the expansion of GAS infection. This idea was also supported by the uptake of [^{35}S]methionine and [^{35}S]cysteine by GAS into Atg5$^{-/-}$ cells but not into the wild-type cells (fig. S3B).

At 4 hours after infection, we observed GcAVs with features characteristic of autophagosomes fused with lysosomes, as observed by electron microscopy: a single membrane–bound compartment and containing degraded cytosol (Fig. 2D) and partially degraded GAS (arrowhead). LC3 and LAMP-1, a lysosomal membrane protein, also colocalized at 2 to 3 hours after infection (Fig. 3, A and B), suggesting fusion with lysosomes after formation of GcAVs, similar to what occurs in the standard autophagic pathway. To examine whether the viability of GAS was impaired by lysosomal enzymes, we performed a bacterial viability assay in the presence of the lysosomal protease inhibitors (Fig. 3C). The decrease of intracellular GAS in wild-type cells was suppressed significantly by treatment with protease inhibitors. In Atg5$^{-/-}$ cells, however, the protease inhibitors did not affect the number of viable intracellular GAS, implying that the decrease in GAS viability requires autophagosome formation and fusion with lysosomes.

GAS is known to secrete streptolysin O (SLO), a member of a conserved family of

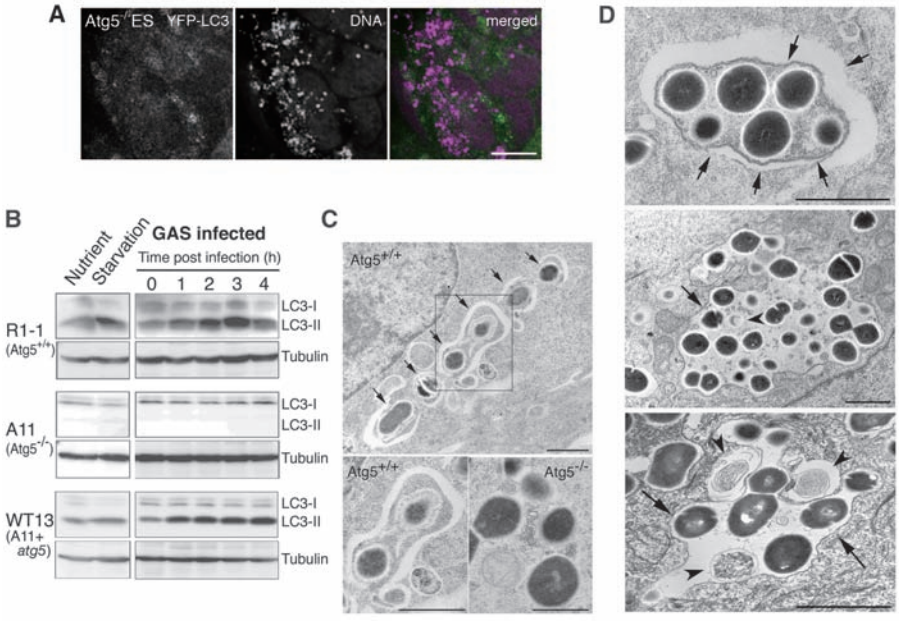

Fig. 2. Atg5 deficiency allows GAS survival within host cells. (**A**) Intracellular GAS were not acquired by LC3-positive compartments in Atg5-deficient ES cells at 3 hours after infection. Yellow fluorescent protein (YFP)–LC3, green; PI-stained DNA, magenta. Bar, 10 μm. (**B**) LC3-II was not formed after GAS infection of Atg5$^{-/-}$ ES cells (A11) but formed in Atg5$^{+/+}$ (R1) and *Atg5* cDNA transformant of A11 (WT13). (**C**) Ultrastructural observations of GAS-infected Atg5$^{+/+}$ ES cells and Atg5$^{-/-}$ ES cells. The lower left panel is the magnified image of the area indicated by the box in the upper panel. Arrows indicate the cisternae surrounding naked GAS. Bars, 1 μm. (**D**) Ultrastructural observations of GAS-infected HeLa cells. We observed the multiple-membrane–bound compartment containing intact cytosol and GAS at 1 hour after infection (upper panel) and the single membrane–bound compartment with degraded cytosol and GAS (arrowhead) at 4 hours after infection (middle and lower panels). Arrows indicate the membranes of the compartments. Bars, 1 μm. (**E**) Viability of intracellular GAS in Atg5$^{+/+}$ (closed symbols) and Atg5$^{-/-}$ (open symbols) cells was measured in the presence (squares) or absence (circles) of tannic acid (TA; final concentration, 0.5%) (9). Data are representative of at least three independent experiments. *$P < 0.01$.

cholesterol-dependent pore-forming cytolysins (*11*). Although the role of SLO is not clear, we found that the intracellular fate of JRS4Δ*SLO*, an isogenic SLO-deficient mutant of strain JRS4, differed from that of the wild type. At early stages (−0.5 and 0 hours) after infection, GAS often colocalized with the early endosome marker, the FYVE domain of EEA-1 (Fig. 4, A and C; fig. S4) (*12*), demonstrating that GAS first enter into endosomes. Then, at 1 hour after infection, endosomes containing GAS gradually disappeared (Fig. 4C). In contrast to the wild-type strain, most JRS4Δ*SLO* cells remained within FYVE-positive compartments even at 2 hours after infection (Fig. 4, A and C), suggesting that JRS4Δ*SLO* failed to escape from endosomes. Furthermore, only a few GcAVs were observed in the JRS4Δ*SLO*-infected cells (Fig. 4, B and D). Taken together with the ultrastructural observation (Fig. 2C), we suggest that GAS escapes from endosomes via a SLO-dependent mechanism and that its entry into the cytoplasm induces autophagy and entrapment of GAS in autophagosome-like compartments.

In keratinocytes, more than 80% of the internalized GAS are killed by 4 hours after infection, and the organisms continue to die over the next 18 hours until they reach ~1% of their original numbers (*13*). Here, killing of GAS during the early phase (by 4 hours of after infection) was solely due to autophagic activity. At 24 hours after GAS infection, ~50% of the infected cells induced apoptosis (*13*), suggesting that the autophagic killing of GAS is not protective toward the cells. However, autophagy is likely to contribute to suppression of GAS virulence, because killing of GAS inside cells results in a reduction of extracellular GAS that is hazardous and cytotoxic for host tissues and cells (*14*). Indeed, decreased invasion rates of GAS in fibronectin-deficient mice results in an increased mortality rate (*15*). Severe and invasive diseases caused by GAS might thus be induced by the attenuation of autophagic activity.

Several bacterial species, including *Rickettsia conorii* (*16*), *Listeria monocytogenes* (*17*), *Porphyromonas gingivalis* (*18*), *Brucella abortus* (*19*), and *Legionella pneumophila* (*20*), reside within double-membrane–bound compartments resembling autophagosomes after the invasion of host cells (*21*). However, the significance of this localization has not been clear. Here we have demonstrated that autophagy can play a role in bacterial invasion of host cells.

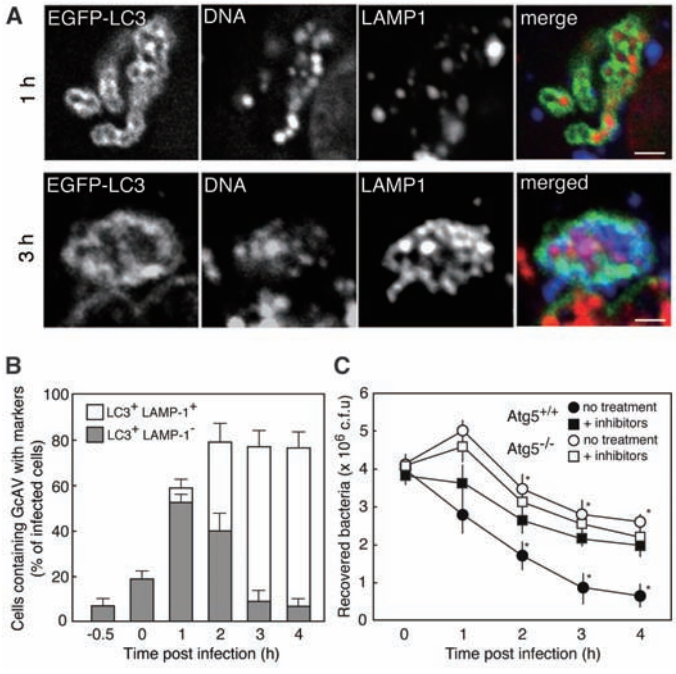

Fig. 3. Fusion of GcAVs with lysosomes. (**A**) Confocal microscopic images of GAS (red)–containing LC3-positive compartments (green) fused with lysosomes (blue). After fixation, lysosomes were stained with an antibody to LAMP-1 (blue). Bars, 2 μm. (**B**) Increase of GcAVs fused with lysosomes with time. After fixation, cells were stained with an antibody to LAMP-1. The numbers of cells, including LAMP-1–positive or –negative GcAVs, was counted (means ± SE, $n = 20$). (**C**) Decrease of intracellular GAS in Atg5$^{+/+}$ cells was inhibited by addition of the lysosomal enzyme inhibitors (+inhibitors; 1 mg/ml of leupeptin and 10 μM E64d). The numbers of intracellular GAS were determined by bacterial viability assay (mean CFU ± SE). Data are representative of at least three independent experiments. *$P < 0.01$.

References and Notes

1. N. Mizushima, Y. Ohsumi, T. Yoshimori, *Cell Struct. Funct.* **27**, 421 (2002).
2. C. W. Wang, D. J. Klionsky, *Mol. Med.* **9**, 65 (2003).
3. T. Yoshimori, *Biochem. Biophys. Res. Commun.* **313**, 453 (2004).
4. A. L. Bisno, M. O. Brito, C. M. Collins, *Lancet Infect. Dis.* **3**, 191 (2003).
5. G. Molinari, M. Rohde, C. A. Guzman, G. S. Chhatwal, *Cell. Microbiol.* **2**, 145 (2000).
6. I. Nakagawa, M. Nakata, S. Kawabata, S. Hamada, *Cell. Microbiol.* **3**, 395 (2001).
7. N. Mizushima *et al.*, *J. Cell Biol.* **152**, 657 (2001).
8. Y. Kabeya *et al.*, *EMBO J.* **19**, 5720 (2000).

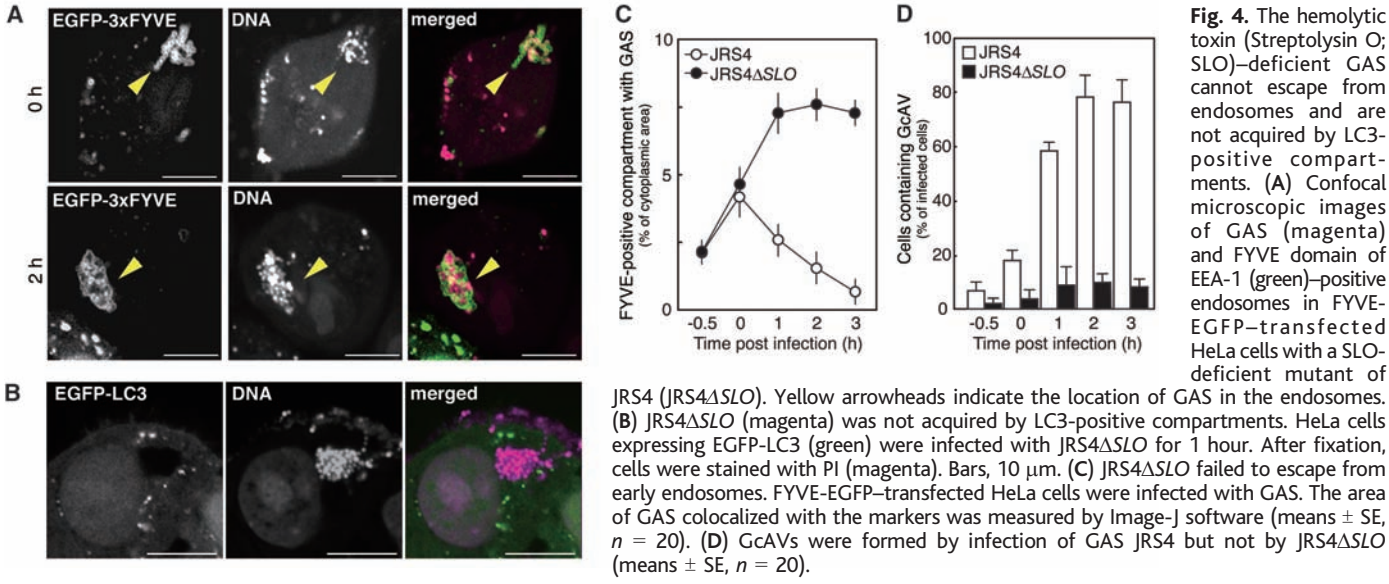

Fig. 4. The hemolytic toxin (Streptolysin O; SLO)–deficient GAS cannot escape from endosomes and are not acquired by LC3-positive compartments. (**A**) Confocal microscopic images of GAS (magenta) and FYVE domain of EEA-1 (green)–positive endosomes in FYVE-EGFP–transfected HeLa cells with a SLO-deficient mutant of JRS4 (JRS4Δ*SLO*). Yellow arrowheads indicate the location of GAS in the endosomes. (**B**) JRS4Δ*SLO* (magenta) was not acquired by LC3-positive compartments. HeLa cells expressing EGFP-LC3 (green) were infected with JRS4Δ*SLO* for 1 hour. After fixation, cells were stained with PI (magenta). Bars, 10 μm. (**C**) JRS4Δ*SLO* failed to escape from early endosomes. FYVE-EGFP–transfected HeLa cells were infected with GAS. The area of GAS colocalized with the markers was measured by Image-J software (means ± SE, $n = 20$). (**D**) GcAVs were formed by infection of GAS JRS4 but not by JRS4Δ*SLO* (means ± SE, $n = 20$).

9. Materials and methods are available as supporting material on *Science* Online.
10. R. Polishchuk, A. Di Pentima, J. Lippencott-Schwartz, *Nat. Cell Biol.* **6**, 297 (2004).
11. R. K. Tweten, in *Virulence Mechanisms of Bacterial Pathogens*, J. A. Roth *et al.*, Eds. (American Society for Microbiology, Washington, DC, 1995), pp. 207–230.
12. J. M. Gaullier, E. Ronning, D. J. Gilloly, H. Stenmark, *J. Biol. Chem.* **275**, 24595 (2000).
13. H. M. Schrager, J. G. Rheinwald, M. R. Wessels, *J. Clin. Invest.* **98**, 1954 (1996).
14. C. Cywes, M. R. Wessels, *Nature* **414**, 648 (2001).
15. P. Nyberg *et al.*, *EMBO J.* **23**, 2166 (2004).
16. D. H. Walker, V. L. Popov, P. A. Crocquet-Valdes, C. J. Welsh, H. M. Feng, *Lab. Invest.* **76**, 129 (1997).
17. K. A. Rich, C. Burkett, P. Webster, *Cell. Microbiol.* **5**, 455 (2003).
18. B. R. Dorn, W. A. Dunn, A. Progulske-Fox, *Infect. Immun.* **69**, 5698 (2001).
19. J. Pizarro-Cerda, E. Moreno, V. Sanguedolce, J. L. Mege, J. P. Gorvel, *Infect. Immun.* **66**, 2387 (1998).
20. S. Sturgill-Koszycki, M. S. Swanson, *J. Exp. Med.* **192**, 1261 (2000).
21. K. Kirkegaard, M. P. Taylor, W. T. Jackson, *Nat. Rev. Microbiol.* **2**, 301 (2004).
22. We thank M. Yaffe for providing 3xFYVE-EGFP plasmid. We also thank T. Tokuhisa, M. Hatano, and A. Kuma for generating the wild-type and Atg5$^{-/-}$ MEF cell lines. This work was supported in part by Grants-in-Aid and 21st Century Center of Excellence (COE) program at Osaka University Graduate School of Dentistry from the Ministry of Education, Culture, Sports, Science and Technology in Japan.

Supporting Online Material
www.sciencemag.org/cgi/content/full/306/5698/1037/DC1
Materials and Methods
Figs. S1 to S4
References
Movie S1

12 August 2004; accepted 4 October 2004

Structural Insights into the Assembly of the Type III Secretion Needle Complex

Thomas C. Marlovits,[1,2] Tomoko Kubori,[2] Anand Sukhan,[2*] Dennis R. Thomas,[3] Jorge E. Galán,[2] Vinzenz M. Unger[1†]

Type III secretion systems (TTSSs) mediate translocation of virulence factors into host cells. We report the 17-angstrom resolution structures of a central component of *Salmonella typhimurium* TTSS, the needle complex, and its assembly precursor, the bacterial envelope–anchored base. Both the base and the fully assembled needle complex adopted multiple oligomeric states in vivo, and needle assembly was accompanied by recruitment of the protein PrgJ as a structural component of the base. Moreover, conformational changes during needle assembly created scaffolds for anchoring both PrgJ and the needle substructure and may provide the basis for substrate-specificity switching during type III secretion.

Type III secretion systems (TTSSs) are central to the virulence of many Gram-negative bacteria pathogenic for animals and plants (*1*, *2*). In addition to the needle complex (*3*), which is the core component of these systems, TTSSs are composed of more than 20 proteins, including a highly conserved group of integral membrane proteins, a family of customized cytoplasmic chaperones, and several accessory proteins (*1*, *2*), placing TTSSs among the most complex protein secretion systems known. In *S. typhimurium*, the needle complex is formed by a base and a filamentous needle, composed of a single protein, PrgI, that projects ~50 nm from the bacterial surface (Fig. 1, A and B) (*3*). The base is formed by InvG, PrgH, and PrgK (*4*) and features four distinct rings, two associated with the outer membrane (OR1 and OR2 in Fig. 1A) and another two that are in close proximity to the inner membrane (IR1 and IR2 in Fig. 1A). The entire complex is essential for virulence (*5*) and is believed to provide a conduit for the direct transport of proteins from the bacterial cytoplasm to the host cell. Here, we have used electron cryomicroscopy to visualize the detailed structural organization of the *S. typhimurium* needle complex, as well as structural changes that occur during the last step of its assembly.

Quantitative amino acid analysis revealed that the components of the base, InvG:PrgH:PrgK, were present in 1:1:1 molar ratios [fig. S1 (*6*)], suggesting that the three proteins were structurally linked by a shared rotational symmetry. Our attempts to determine this symmetry by labeling the base with antibodies or gold, as well as by scanning transmission electron microscopy analysis, all yielded ambiguous results (*7*). Moreover, the resolution in several reconstructions stalled at ~30 Å despite increasing the number of particle images in the data sets. This suggested sample heterogeneity. To test whether the heterogeneity was caused by different rotational symmetries, we used a

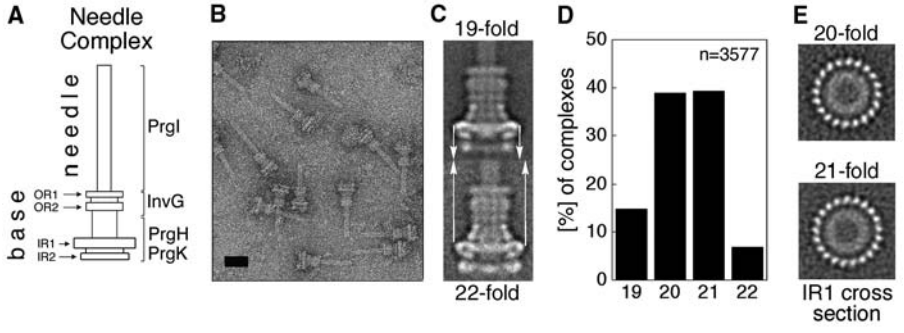

Fig. 1. The needle complex and the base complex of the TTSS from *S. typhimurium* can adopt different symmetries in vivo. (**A**) Nomenclature of the structural features of the needle complex. The needle complex is divided into two distinctive substructures: the membrane-embedded base and the extracellular needle filament. The base spans the periplasm and is associated with the inner and outer membranes, where ringlike structures are visible in electron micrographs of negatively stained needle complexes (2% phosphotungstic acid, pH 7) (**B**). The outer membrane–associated rings (OR1 and OR2) are composed of the protein InvG, and the inner membrane–associated rings (IR1 and IR2) contain the proteins PrgH and PrgK (*4*). The only protein identified for the needle filament to date is PrgI (*4*). Bar, 30 nm. (**C**) Model-based multireference alignment revealed significant differences in the diameters of the average projections obtained for different rotational symmetries, as indicated by white arrows in the comparison of the IR1 of the 19- and 22-fold particles. (**D**) Distribution of different symmetries in needle complexes isolated from wild-type *S. typhimurium*. The data were generated by examining 3577 particles. (**E**) After sorting of the particles and 3D reconstruction without enforcing any symmetry, the true rotational symmetries could be derived from cross sections through IR1 of the reconstructed needle complexes, as shown for the 20- and 21-fold particles.

[1]Department of Molecular Biophysics and Biochemistry, Yale University School of Medicine, New Haven, CT 06520–8024, USA. [2]Section of Microbial Pathogenesis, Yale University School of Medicine, New Haven, CT 06536, USA. [3]Rosenstiel Basic Medical Sciences Research Center, Brandeis University, Waltham, MA 02454, USA.

*Present address: Department of Microbiology, Oklahoma State University, Stillwater, OK 74078, USA.
†To whom correspondence should be addressed. E-mail: vinzenz.unger@yale.edu